

A comparative study of the centroid and ring-polymer molecular dynamics methods for approximating quantum time correlation functions from path integrals

Alejandro Pérez,¹ Mark E. Tuckerman,^{2,a)} and Martin H. Müser^{3,b)}¹Department of Chemistry, New York University, New York, New York 10003, USA²Department of Chemistry and Courant Institute of Mathematical Sciences, New York University, New York, New York 10003, USA³Department of Applied Mathematics, University of Western Ontario, London, Ontario N6A 5B7, Canada

(Received 1 October 2008; accepted 9 April 2009; published online 12 May 2009)

The problems of ergodicity and internal consistency in the centroid and ring-polymer molecular dynamics methods are addressed in the context of a comparative study of the two methods. Enhanced sampling in ring-polymer molecular dynamics (RPMD) is achieved by first performing an equilibrium path integral calculation and then launching RPMD trajectories from selected, stochastically independent equilibrium configurations. It is shown that this approach converges more rapidly than periodic resampling of velocities from a single long RPMD run. Dynamical quantities obtained from RPMD and centroid molecular dynamics (CMD) are compared to exact results for a variety of model systems. Fully converged results for correlations functions are presented for several one dimensional systems and *para*-hydrogen near its triple point using an improved sampling technique. Our results indicate that CMD shows very similar performance to RPMD. The quality of each method is further assessed via a new χ^2 descriptor constructed by transforming approximate real-time correlation functions from CMD and RPMD trajectories to imaginary time and comparing these to numerically exact imaginary time correlation functions. For *para*-hydrogen near its triple point, it is found that adiabatic CMD and RPMD both have similar χ^2 error. © 2009 American Institute of Physics. [DOI: 10.1063/1.3126950]

I. INTRODUCTION

Solving the quantum dynamics of many-body systems remains one of the most challenging problems in computational physics and chemistry due to the unfavorable computer scaling with system size and time scale of numerically exact methods. Quantum equilibrium properties, on the other hand, are routinely investigated using the path integral (PI) formalism developed by Feynman.^{1,2} The PI interpretation fostered a new understanding of the microscopic world and provided a deep insight into various complex quantum phenomena, such as superfluidity.³ Unfortunately, direct application of this formalism to real-time dynamics faces a severe *sign problem* that necessitates approximation schemes.

In the past decades, several approaches have been developed to describe approximately the dynamics of quantum systems, which include the linearized semiclassical initial value representation of Liu and Miller,^{4,5} the quantum mode coupling theory of Reichman and Rabani,^{6–10} the forward-backward approach of Nakayama and Makri,^{11,12} the Feynman–Kleinert linearized PI method,¹³ and the effective potential analytic continuation method,¹⁴ among others.

In the quest for simplifications to the finite-temperature quantum dynamics problem, much research effort has been directed toward devising quasiclassical approaches. Among

these, centroid molecular dynamics (CMD) developed by Cao and Voth¹⁵ attracted much attention in the past decade. The method was successfully applied to a wide variety of model systems,¹⁶ and it represents a promising avenue in condensed matter physics.

In the past few years, the field of quasiclassical methods has burgeoned with recent advances in approximate methods to the quantum dynamics problem.^{17,18} Recently, Craig and Manolopoulos¹⁹ revived the primitive PI algorithm²⁰ and applied it to approximate a variety of dynamical properties. The method has been termed ring-polymer molecular dynamics (RPMD).¹⁹

A subsequent study by Braams and Manolopoulos²¹ showed analytically that Kubo-transformed autocorrelations functions obtained from RPMD are accurate up to $\mathcal{O}(t^6)$ for the position and $\mathcal{O}(t^4)$ for the velocity, while the (adiabatic) CMD leads to an accuracy of only $\mathcal{O}(t^4)$ and $\mathcal{O}(t^2)$ for the position and velocity, respectively. Although these analytical results are clear, how they manifest in actual many-body simulations remains an open question, particularly considering that there are differences between the protocols used in the theoretical analysis and those used in actual applications, as will be discussed further below.

Recently, Hone *et al.*²² compared CMD and RPMD on a variety of model systems. Their study reached the conclusion that both approaches yield similar results in condensed phases although some marked differences were detected for

^{a)}Electronic mail: mark.tuckerman@nyu.edu. URL: <http://homepages.nyu.edu/~mt33/>.

^{b)}Electronic mail: mmuser@uwo.ca. URL: <http://publish.uwo.ca/~mmuser/>.

low dimensional model systems. The authors found that increasing the time separation between the centroid and the internal modes brings CMD closer to the exact results, leading to better estimates for the diffusion constant of *para*-hydrogen than RPMD.²² Moreover, better estimates of the quantum kinetic energy (from the zero time of the velocity autocorrelation function) for the same system were obtained in CMD than in RPMD. These findings partially obscure the aforementioned analysis by Braams and Manolopoulos.²¹

A potential weakness exists in each of the two aforementioned studies, which may lie at the origin of this discrepancy: The argument of Braams and Manolopoulos that CMD is less accurate at short times than RPMD assumes that the CMD is entirely Newtonian, i.e., the dynamics of internal and centroid modes are governed only by a mass tensor. However, in actual CMD simulations, thermostats are typically applied to the noncentroid modes of the ring polymer for equilibration, rendering the motion of internal modes non-Newtonian (but with increased sampling efficiency). At the same time, Hone *et al.*²² did not employ an optimal sampling of RPMD in their numerical comparison. It is well known that RPMD suffers from long correlation times and naïve resampling of velocities from an equilibrium distribution (as was done in Ref. 22) can easily hinder the acquisition of optimal RPMD time correlation functions.

In this comparative study, we re-examine several model systems, together with new ones, with the intention of achieving optimal sampling in both approaches. To this end, an improved sampling technique in RPMD is introduced in order to ensure more rapid convergence of the correlation functions.

In addition to improving the sampling, we also introduce an internal consistency check to assess the quality of each PI approach. When evaluating each approach, it is desirable to have a quantitative descriptor of the method's performance, irrespective of the availability of a numerically exact solution of the dynamical problem. While for low dimensional systems, one can easily compare approximate results to those obtained by numerically exact methods, no such comparison is possible for high dimensional, nonharmonic systems such as liquid *para*-hydrogen.

In complex systems, comparison with experimental data as a means of assessing the accuracy of a quantum dynamical approach is problematic, as there is no guarantee that the force field employed is sufficiently accurate. Agreement between a computational prediction and experimental measurement could be due to a fortuitous cancellation of errors in the method and/or force field. This last statement could easily apply to model Hamiltonians that treat a linear molecule as a spherical particle and thus neglect translation-rotation coupling. This translation-rotation coupling as well as three-body forces are likely to affect different observables in different ways so that experiments and simulations cannot be expected to match with high accuracy.^{23,24} By the same argument, if the calculation and experiment do not agree, it is often difficult to discern how much this discrepancy is due to the quantum dynamics approximation and how much to the force field. It is worth noting, however, that in a very recent study by Witt *et al.*,⁶⁵ the authors showed that both RPMD

and CMD leave very definite artifacts in vibrational spectra, particularly, at low temperatures, due to insufficient decoupling of physical vibrational modes and vibrational modes of the cyclic polymer chain in RPMD or distortions of the 'effective classical potential' generated in CMD (see Fig. 5 of Ref. 65).

A more consistent test, therefore, would be to use the fact that the information contained in the imaginary time correlation function is equivalent to that contained in the real-time correlation function.²⁵ Numerically exact imaginary time correlation functions are easily computed from either PIMD or PI Monte Carlo, even for complex systems, assuming an efficient PI sampling approach. Unfortunately, the transformation from imaginary time to real time is numerically ill posed, which makes a direct test of the estimates for the real-time correlation functions a complicated task,²⁶ in some cases possible^{27–29} but more commonly, inaccurate.^{10,30} Nevertheless, the transformation from real time to imaginary time is numerically stable and can be used as a consistency check. This allows us to pose the following question:³¹ How accurately do CMD or RPMD predict imaginary time correlation functions if these functions are not averaged directly but determined indirectly via the approximate real-time autocorrelation functions? This comparison allows us to assess the quality of a method by means of a well-defined descriptor (to be defined later) without relying on the accuracy of the model potential.

This article is organized as follows: Sec. II A reviews the equilibrium PI methodology of Ref. 32. Sec. II B presents a brief review on the formalism on quantum correlation functions. This is followed by a succinct description of the approximate imaginary time PI methods CMD (Sec. II C), RPMD (Sec. II D), and its representation in other coordinates (Sec. II E). The theory section ends with a discussion of the ergodic problems in PIs, our proposed sampling scheme (Sec. II F), and with the new quantitative descriptor (Sec. II G). In the accompanying Sec. III, the model systems and relevant technical details are presented. The article continues in Sec. IV with a discussion of the main results. Finally, the conclusions are drawn in Sec. V.

II. BACKGROUND AND THEORY

A. Equilibrium path integral molecular dynamics

In this section, we briefly review the methodology of PIMD. In the proceeding, \hat{H} will denote the Hamiltonian operator of the system, $\beta=1/k_B T$ is the inverse thermal energy, and $Z(\beta)=\text{Tr} \exp(-\beta\hat{H})$ is the canonical quantum partition function.

The discrete PI expression for the quantum canonical partition function for a single particle of mass m with Hamiltonian $\hat{H}=\hat{p}^2/2m+V(\hat{x})$ is

$$Z_P(\beta) = \left(\frac{mP}{2\pi\beta\hbar^2} \right)^{P/2} \int dx_1, \dots, dx_P \times \exp \left\{ -\beta \sum_{k=1}^P \left[\frac{1}{2} m \omega_P^2 (x_k - x_{k+1})^2 + \frac{1}{P} V(x_k) \right] \right\}, \quad (1)$$

where $\omega_P = \sqrt{P}/(\beta\hbar)$ and P is the Trotter number or number of imaginary time slices along the thermal path. The paths must satisfy the cyclic condition $x_{P+1} = x_1$, which arises from the trace.

Without changing any of the thermodynamic or equilibrium properties of the system, we can introduce a set of P uncoupled Gaussian integrals into Eq. (2) as follows:

$$Z_P(\beta) = \mathcal{N} \int dp_1, \dots, dp_P \int dx_1, \dots, dx_P \times \exp \left\{ -\beta \sum_{k=1}^P \left[\frac{p_k^2}{2m'_k} + \frac{1}{2} m \omega_P^2 (x_k - x_{k+1})^2 + \frac{1}{P} V(x_k) \right] \right\}, \quad (2)$$

where m'_k are fictitious mass parameters and \mathcal{N} is an overall normalization constant. In principle, the quantum canonical partition function could be computed via MD using the following classical Hamiltonian:

$$H = \sum_{k=1}^P \left[\frac{p_k^2}{2m'_k} + \frac{1}{2} m \omega_P^2 (x_k - x_{k+1})^2 + \frac{1}{P} V(x_k) \right], \quad (3)$$

which describes the motion of a cyclic polymer chain with harmonic nearest-neighbor interactions in an attenuated external potential $V(x)/P$.^{33,34} Because of the resemblance of the cyclic polymer to a necklace, the imaginary time points are colloquially referred to as “beads,” and the variables $\mathbf{x} = x_1, \dots, x_P$ are referred to as the “primitive” PI variables. The parameters m'_k determine the time scale on which the imaginary time points x_1, \dots, x_P are sampled. However, as was pointed by Hall and Berne,³⁵ the efficiency of the primitive algorithm is very poor due to the dominance of the harmonic forces from the quantum kinetic energy. Even if thermostats are coupled to each degree of freedom in the system, the wide frequency spectrum introduced by the harmonic coupling causes the MD time step to be limited by the fast modes, thereby leading to very poor sampling of the low-frequency modes.

A solution to the aforementioned problem was introduced by Tuckerman *et al.*³² and consists of three elements: (1) the variables in Eq. (3) are transformed to a set of coordinates that diagonalizes the harmonic coupling; (2) the fictitious masses m'_k are adjusted so that all modes move on the same time scale; (3) a thermostat is coupled to each mode degree of freedom in the system so as to ensure rapid sampling, equipartitioning, and a proper canonical distribution.

The equations for the transformation from primitive to a new set of so-called “staging” modes³² can be derived from

similar transformations used in PI Monte Carlo.³⁶ In its simplest form, the transformation to staging modes q_1, \dots, q_P (denoted collectively by \mathbf{Q}) is

$$q_1 = x_1, \\ q_k = x_k - \frac{(k-1)x_{k+1} + x_1}{k}, \quad k = 2, \dots, P. \quad (4)$$

Note that this transformation is a special case of a more general staging transformation discussed in Ref. 32. When the change in variables given by Eq. (4) is introduced into Eq. (3), the partition function becomes

$$Z_P(\beta) = \mathcal{N} \int dp_1, \dots, dp_P \int dq_1, \dots, dq_P \times \exp \left\{ -\beta \sum_{k=1}^P \left[\frac{p_k^2}{2m'_k} + \frac{1}{2} m_k \omega_P^2 q_k^2 + \frac{1}{P} V(x_k(\{\mathbf{Q}\})) \right] \right\}, \quad (5)$$

where $x_k(\{\mathbf{Q}\})$ indicates the inverse transformation, and the masses m_k are defined to be

$$m_1 = 0, \\ m_k = \frac{k}{k-1} m, \quad k = 2, \dots, P. \quad (6)$$

Note that by this definition, the mode variable q_1 drops out of the quantum kinetic energy term so that its motion is solely governed by the external potential V . In order to ensure that all modes move on the same time scale, the fictitious masses m'_k are chosen according to $m'_1 = m$ and $m'_k = m_k$. Therefore, PIMD in staging modes is defined by the transformed Hamiltonian

$$H_{\text{stage}} = \sum_{k=1}^P \left[\frac{p_k^2}{2m'_k} + \frac{1}{2} m_k \omega_P^2 q_k^2 + \frac{1}{P} V(x_k(\{\mathbf{Q}\})) \right]. \quad (7)$$

In Eq. (7), the momenta p_k are treated as “conjugate” to the mode variables q_k , which means that the dynamics generated by Eqs. (7) and (3) are different because the transformation is not canonical. This freedom of choosing the fictitious masses is permitted as far as equilibrium thermodynamic quantities are concerned (however not so in dynamical algorithms as discussed in Sec. II E). Finally, once the equations of motion (EOMs) are derived using Eq. (7), each mode variable is coupled to a separate thermostat, e.g., a Nosé–Hoover chain thermostat.³⁷ In Ref. 32, a more general staging type of approach was introduced by allowing staging “segments” of length j to be defined, thereby providing a natural cutoff between fast and slow modes, a generalization that was shown to possess certain advantages regarding the convergence of PIs with large P .

The authors of Ref. 32 also suggested that the same scheme could be used with normal mode (NM) variables: “The staging method handles the [time-step] problem by introduction of the variable j , which naturally classifies the

modes and allows only those with wavelength smaller than some cutoff to fluctuate rapidly. Such a division of time scales based on wavelength can also be constructed using normal modes.” This idea was subsequently implemented by Cao and Voth³⁸ in the context of CMD (see below), by Tuckerman *et al.*,³⁹ in *ab initio* PIs methods, by Marx *et al.*⁴⁰ in *ab initio* CMD algorithms, and by Martyna *et al.*⁴¹ in the context of PIs at constant pressure. The transformation in this case takes the form

$$q_k = \frac{1}{\sqrt{P}} \sum_{i=1}^P U_{ki} x_i, \quad (8)$$

where the transformation U_{ki} diagonalizes the matrix arising from the quantum kinetic part: $A_{ij} = 2\delta_{ij} - \delta_{i,j-1} - \delta_{i,j+1}$ with $A_{i,P+1} = A_{i1}$ and $A_{j0} = A_{jP}$. Introducing this change in variables in Eq. (3) yields a partition function that has the same form as Eq. (6) but with

$$m_k = m\lambda_k, \quad (9)$$

$$\lambda_{2k-1} = \lambda_{2k-2} = 2P \left[1 - \cos\left(\frac{2\pi(k-1)}{P}\right) \right],$$

and $\lambda_1 = 0$, $\lambda_P = 4P$ (for even P). As with the staging transformation, the mode q_1 drops out of the quantum kinetic energy term. In fact, it is the centroid mode, x_0 ,

$$q_1 = x_0 = \frac{1}{P} \sum_{i=1}^P x_i. \quad (10)$$

In order to ensure that all modes move on the same time scale, the fictitious masses m'_k are chosen according to $m'_k = m_k$ and $m'_1 = m$, which is the optimal choice for the free particle. However, depending on the system, other choices for the kinetic masses may be more efficient.⁴² As in the staging case, each NM degree of freedom is also coupled to its own thermostat.

The schemes reviewed in this section have proved highly useful in equilibrium PIMD and have made the PACMD scheme to be discussed in Sec. II C possible.

B. Quantum time correlation functions

In this section, some general aspects of quantum correlation functions are succinctly reviewed.^{26,43} The standard quantum time correlation function is defined by

$$C_{AB}(t) = \langle \hat{A}(0) \hat{B}(t) \rangle, \quad (11)$$

where \hat{A} and \hat{B} are quantum mechanical operators in the Heisenberg picture. The angular brackets denote the thermal average

$$\langle \hat{O} \rangle = \frac{1}{Z(\beta)} \text{Tr}[\hat{O} \exp(-\beta\hat{H})]. \quad (12)$$

In contrast to their totally symmetric classical counterparts, standard quantum correlation functions C_{AB} obey the detailed balance relation in Fourier space: $\tilde{C}_{AB}(-\omega) = \tilde{C}_{AB}(\omega) e^{-\beta\hbar\omega}$.

It is often more convenient, however, to work with the

so-called Kubo-transformed correlation function⁴⁴

$$K_{AB}(t) = \frac{1}{\beta Z(\beta)} \int_0^\beta d\lambda \text{Tr}[e^{-(\beta-\lambda)\hat{H}} \hat{A} e^{-\lambda\hat{H}} e^{i\hat{H}t/\hbar} \hat{B} e^{-i\hat{H}t/\hbar}], \quad (13)$$

than with the original $C_{AB}(t)$ for several reasons: First, $K_{AB}(t)$ is purely real and invariant under time reversal. Thus, it exhibits more symmetry properties than $C_{AB}(t)$. Consequently, many exact expressions for $K_{AB}(t)$ become relatively compact. Second, $K_{AB}(t)$ is more easily compared to classical time correlation functions, which are the natural output of both CMD and RPMD calculations. Third, in the linear regime, the response of the system is directly linked to such functions via the Kubo relations.⁴⁵ Finally, $K_{AB}(t)$ reduces to its classical counterpart not only in the classical limit $\beta \rightarrow 0$ but also in harmonic systems. The Kubo-transformed and the standard correlation functions contain the same information and, in Fourier space, are related by

$$\tilde{C}_{AB}(\omega) = \left[\frac{\beta\hbar\omega}{1 - e^{-\beta\hbar\omega}} \right] \tilde{K}_{AB}(\omega). \quad (14)$$

A quantity that is typically computed in PI simulations is the imaginary time quantum correlation function

$$G_{AB}(\tau) = \frac{1}{Z(\beta)} \text{Tr}[e^{-\beta\hat{H}} \hat{A} e^{-\tau\hat{H}/\hbar} \hat{B} e^{\tau\hat{H}/\hbar}], \quad (15)$$

which follows from Eq. (11) after an analytic continuation to imaginary time. In particular, the imaginary time mean square displacement is easily computed from PIMD/PIMC simulations, even for complex systems

$$G(\tau) = \langle [x(\tau) - x(0)]^2 \rangle. \quad (16)$$

This important quantity is related to the real-time velocity autocorrelation function $C_{vv}(t)$ (more precisely, its Fourier transform $\tilde{C}_{vv}(\omega)$) via a two-sided Laplace transform

$$G(\tau) = \frac{1}{\pi} \int_{-\infty}^{\infty} d\omega \exp(-\beta\hbar\omega/2) \frac{\tilde{C}_{vv}(\omega)}{\omega^2} \left\{ \cosh\left[\omega\left(\frac{\beta\hbar}{2} - \tau\right)\right] - \cosh\left(\frac{\beta\hbar\omega}{2}\right) \right\}. \quad (17)$$

This last equation will be used in Sec. II G to assess the virtues of each imaginary time method.

C. Centroid molecular dynamics

In 1993, Cao and Voth¹⁵ introduced CMD as an approximate method to compute real-time quantum correlation functions. The primary object in this approach is the centroid,³³ defined as the average of the cyclic path $x(\tau)$ in imaginary time τ [see also Eq. (10)],

$$x_0[x(\tau)] = \frac{1}{\beta\hbar} \int_0^{\beta\hbar} x(\tau) d\tau \approx \frac{1}{P} \sum_{i=1}^P x(\tau_i). \quad (18)$$

In Eq. (18) the continuous version is also approximated by a discretization over P imaginary time points [see also

Eq. (10)]. The method is rooted in the ideas developed by Feynman and Kleinert⁴⁶ on the effective centroid potential, which is just a potential of mean force obtained by integrating over the NM variables q_2, \dots, q_P defined in Eq. (8), and of Gillan,⁴⁷ who generalized the Feynman path concept to observables arising from time-dependent processes.

CMD relies on the assumption that the time evolution of the centroid on this potential of mean force surface can be used to garner approximate quantum dynamical properties of a system. In CMD, the centroid evolves in time according to Newtonian EOMs (Refs. 16 and 48)

$$\dot{x}_c = \frac{p_c}{m}, \quad (19)$$

$$F_0(x_c) = - \frac{\oint \mathcal{D}x(\tau) \delta(x_0[x(\tau)] - x_c) \left[\frac{1}{\beta\hbar} \int_0^{\beta\hbar} \frac{dV}{dx(\tau')} d\tau' \right] e^{-S[x(\tau)]/\hbar}}{\oint \mathcal{D}x(\tau) \delta(x_0[x(\tau)] - x_c) e^{-S[x(\tau)]/\hbar}}. \quad (21)$$

Although formally exact within the CMD framework, Eqs. (20) and (21) are of limited use. In principle, their evaluation entails a full PI calculation at each centroid configuration, which clearly is not feasible for complex systems.

To ameliorate the computational burden of Eqs. (20) and (21) in practical MD calculations, the adiabatic approximation is often invoked.⁴⁹ The masses of the internal modes are made significantly lighter than the centroid mass so as to affect an adiabatic decoupling of the centroid from the remaining modes, a procedure that allows the centroid potential of mean force to be generated “on the fly” as the CMD simulation is carried out as required by Eq. (21). In order to achieve this limit, an adiabaticity parameter γ^2 ($0 < \gamma^2 < 1$) is introduced to scale down the fictitious kinetic masses of the internal modes $m'_k = \gamma^2 m \lambda_k$ and therefore to accelerate their dynamics.²² Reference 40 contains one particular proof of the adiabatic method. In practice, however, a partial separation is normally sufficient, and the scheme has been termed partially adiabatic centroid molecular dynamics (PACMD).²² In this work, however, we obviate this distinction and simply refer to PACMD as CMD for brevity.

Equation (21) also demands a canonical sampling over the internal modes. As discussed in Sec. II A, thermostats are typically attached to the internal (noncentroid) modes to achieve a rapid equilibration whereas the centroid is normally unthermostated so as not to disrupt the dynamical properties of the system. More technical details on the method are discussed in Refs. 40, 41, and 49

Finally, in the CMD formalism, the expectation value of

$$F_0(x_c) \equiv \dot{p}_c = - \frac{dV_0(x_c)}{dx_c},$$

where m is the physical mass, and $V_0(x_c)$ is the mean field potential on the centroid at the point x_c given by

$$V_0(x_c) = - \frac{1}{\beta} \ln \left\{ \left(\frac{2\pi\beta\hbar^2}{m} \right)^{1/2} \oint \mathcal{D}x(\tau) \delta(x_0[x(\tau)] - x_c) e^{-S[x(\tau)]/\hbar} \right\}. \quad (20)$$

In Eq. (20), $S[x(\tau)]$ is the Euclidean time action and $\oint \mathcal{D}x(\tau)$ denotes a functional integration over all cyclic paths, and the δ -function ensures that the paths have centroid position x_c . The mean field centroid force at x_c , $F_0(x_c)$, is derived from Eq. (20) simply by spatial differentiation,

an observable \hat{O} that depends only on position \hat{x} or momentum \hat{p} is expressed as an ensemble average over the centroid variables. Thus, for $\hat{O}(\hat{x})$,

$$\langle \hat{O} \rangle \approx \frac{1}{Z} \int \int \frac{dx_c dp_c}{2\pi\hbar} O(x_c) e^{-\beta[(p_c^2/2m) + V_0(x_c)]}, \quad (22)$$

where $O(x)$ is the eigenvalue of $\hat{O}(\hat{x})$. An analogous definition holds for $\hat{O}(\hat{p})$. In particular, the Kubo-transformed quantum time correlation function between two operators \hat{A} and \hat{B} that are functions only of position \hat{x} is approximated by

$$\langle \hat{A}(0) \hat{B}(t) \rangle \approx \frac{1}{Z} \int \int \frac{dx_c dp_c}{2\pi\hbar} A(x_c(0)) B(x_c(t)) e^{-\beta[(p_c^2/2m) + V_0(x_c)]}, \quad (23)$$

where the function $B(x_c(t))$ is evaluated using the time-evolved centroid variables according to Eq. (20), starting from $\{x_c(0), p_c(0)\}$ as initial conditions. An analogous definition holds for operators \hat{A} and \hat{B} that are functions of momentum only. As discussed by Hernandez, *et al.*,⁵⁰ Eqs. (22) and (23) can be generalized for operators that are functions of both position and momentum using the Weyl operator ordering procedure, however, we will not review this formalism here.

D. Ring polymer molecular dynamics

RPMD starts with the primitive PI algorithm of Eq. (3). In their recent article,¹⁹ Craig and Manolopoulos extended

the primitive method to the real-time domain based on its correct limits in the harmonic and classical cases. The method was later applied to study the self-diffusion of quantum fluids,^{51,52} the inelastic neutron scattering of *para*-hydrogen,⁵³ and to formulate a quantum version of the transition state theory.⁵⁴

The principal differences that distinguish RPMD from CMD are threefold. First, the RPMD kinetic masses are chosen such that each imaginary time slice or bead has the physical mass m . Second, RPMD uses the full chain to estimate expectation values,

$$O_P(t) = \frac{1}{P} \sum_{i=1}^P O(x_i(t)). \quad (24)$$

For example, in RPMD the Kubo-transformed velocity autocorrelation function for a one dimensional system is approximated by

$$K_{vv}(t) \approx \frac{1}{(2\pi\hbar)^P Z_P} \int d\mathbf{x} \int d\mathbf{p} v_P(0) v_P(t) e^{-\beta_P H_P(\mathbf{x}, \mathbf{p})}, \quad (25)$$

where $\beta_P = \beta/P$ (RPMD simulations are typically carried out at P times the actual temperature) and

$$H_P(\mathbf{x}, \mathbf{p}) = \sum_{j=1}^P \frac{p_j^2}{2m} + \frac{m}{2\beta_P^2 \hbar^2} \sum_{j=1}^P (x_j - x_{j-1})^2 + \sum_{j=1}^P V(x_j). \quad (26)$$

Note that the harmonic bead-coupling and potential energy terms are taken to be P times larger than their counterparts in Eq. (3). We adopt this convention for consistency with Ref. 19; however note that this amounts to nothing more than a rescaling of the temperature from T to PT . Obviously, for operators linear in position or momentum, the CMD and RPMD representations of observables are the same, however, they usually differ for functions that are nonlinear in those coordinates.

The third difference is that RPMD is purely Newtonian. The EOMs are easily derived from the previous Hamiltonian, Eq. (26),

$$\dot{p}_j = -\frac{m}{\beta_P^2 \hbar^2} [2x_j - x_{j-1} - x_{j+1}] - \frac{\partial V}{\partial x_j}, \quad (27)$$

$$\dot{x}_j = \frac{p_j}{m},$$

where $j=1, \dots, P$. No thermostats are used on any of the beads because all beads are treated as dynamical variables in RPMD.

E. Ring polymer molecular dynamics in other coordinates

The RPMD scheme presented in the last subsection was defined using Cartesian (or primitive) coordinates [see Eq. (26)] which in compact notation reads

$$H(\mathbf{x}, \mathbf{p}) = \frac{\mathbf{p}^t \mathbf{p}}{2m} + \frac{m}{2} \Omega_P^2 \mathbf{x}^t \kappa \mathbf{x} + V(\mathbf{x}). \quad (28)$$

Here, $\Omega_P^2 = (P/\beta\hbar)^2$ and κ is the stiffness matrix. However, it is possible to carry out the same dynamics using other coordinates provided that the transformation is canonical, i.e., the Poisson brackets are preserved. Unlike in Sec. II A, here not only are the positions changed but the momenta are also transformed accordingly in order to generate the same dynamics, as in Eq. (26). In this subsection, we discuss how the RPMD Hamiltonian transforms using normal mode (NM) and staging coordinates, which are the most commonly used variables in PI calculations.

The NM transformation was introduced in Eq. (8), where U is a unitary matrix with elements $U_{1j} = 1/\sqrt{P}$ and $U_{Pj} = (-1)^j/\sqrt{P}$ for $j=1, \dots, P$; and $U_{2i,j} = \sqrt{2/P} \cos(2\pi ij/P)$ and $U_{2i+1,j} = \sqrt{2/P} \sin(2\pi ij/P)$ for $1 \leq i < P/2$. The RPMD Hamiltonian in NM coordinates reads

$$H(\mathbf{Q}, \mathbf{P}) = \frac{1}{2} \mathbf{\Pi}^t \mathcal{M}^{-1} \mathbf{\Pi} + \frac{m}{2} \Omega_P^2 \mathbf{Q}^t \mathcal{K} \mathbf{Q} + V(\mathbf{x}(\mathbf{Q})), \quad (29)$$

where $\mathbf{\Pi} = \pi_1, \dots, \pi_P$ are the transformed momenta and $\mathcal{M} = mP\mathcal{I}$ is the new mass tensor, with \mathcal{I} the identity matrix. The stiffness matrix in these coordinates $\mathcal{K} = PU\kappa U^t$ (t denotes matrix transpose) becomes diagonal and its elements \mathcal{K}_j are given by Eq. (9). The EOMs generated by this new Hamiltonian are

$$\dot{\pi}_i = -m\Omega_P^2 \mathcal{K}_i q_i - \sqrt{P} \sum_{j=1}^P U_{ij} \nabla_{x_j} V(\mathbf{x}(\mathbf{Q})), \quad (30)$$

$$\dot{q}_i = \sum_{j=1}^P \mathcal{M}_{ij}^{-1} \pi_j = \frac{\pi_i}{mP}.$$

The advantage of using NM coordinates is that the centroid mode separates out naturally and multiple time scale integration methods⁵⁵ can be easily incorporated in the integration scheme of the harmonic kinetic part.⁵¹ Finally, the equipartition theorem, which in Cartesian velocities is $m\langle v^2 \rangle = TP$, now becomes $m\langle \mathbf{V}^t \mathbf{V} \rangle = T$ where $\mathbf{V} = \dot{\mathbf{Q}} = U\dot{\mathbf{x}}/\sqrt{P}$ denotes the NM velocities.

As stated in Sec. II A, one of us³² introduced the staging transformation in PIMD for efficient sampling of equilibrium quantities of quantum system. The staging coordinates are defined by $\mathbf{Q} = \mathcal{T}\mathbf{x}$, with the associated canonical momenta $\mathbf{\Pi} = \mathcal{T}^{-1}\mathbf{p}$. The transformation matrix \mathcal{T} is nonorthogonal, but nonetheless, it accomplishes a total diagonalization of the stiffness matrix κ . The resulting diagonal elements are, however, not the eigenvalues of original matrix κ .

The RPMD Hamiltonian in staging coordinates resembles the one in Eq. (29), except for a new mass tensor $\mathcal{M} = m\mathcal{T}^{-1t}\mathcal{T}^{-1}$, which is symmetric but not diagonal. The new stiffness matrix $\mathcal{K} = \mathcal{T}^{-1t}\kappa\mathcal{T}^{-1}$ becomes diagonal in this representation with elements $\mathcal{K}_i = i/(i-1)$ for $i=2, \dots, P$ and $\mathcal{K}_1=0$. The EOM formulated in staging variables are given by

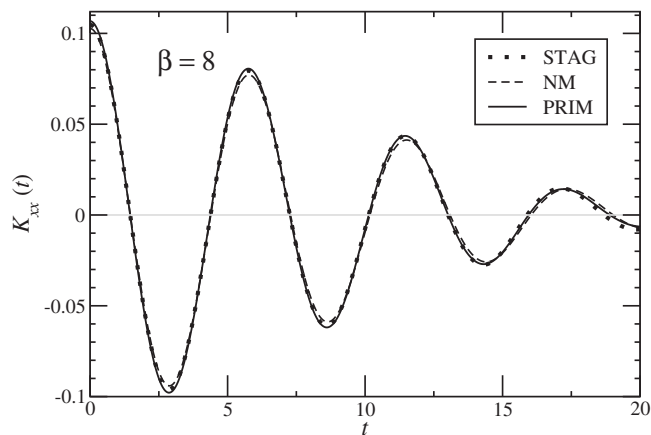


FIG. 1. Kubo-transformed position autocorrelation function for quartic potential $V(x)=0.25x^4$, $\beta=8$, and $P=32$ computed from RPMD in various coordinates: primitive (solid), NMs (dashes), and staging (dots). The minor discrepancies between curves are due to the sampling over many different initial conditions.

$$\begin{aligned} \dot{\pi}_i &= -m\Omega_p^2 \mathcal{K}_i q_i - \sum_{j=1}^P \mathcal{T}_{ij}^{-1} \nabla_{x_j} V(\mathbf{x}(\mathbf{Q})), \\ \dot{q}_i &= \sum_{j=1}^P \mathcal{M}_{ij}^{-1} \pi_j, \end{aligned} \quad (31)$$

where $\mathcal{M}^{-1} = m^{-1} \mathcal{T} \mathcal{T}^T$ is the inverse mass tensor in staging variables. Finally, the equipartition theorem in staging velocities reads $\langle \mathbf{V}^T \mathcal{M} \mathbf{V} \rangle = PT$.

Figure 1 displays the Kubo-transformed position autocorrelation function for the quartic potential $0.25x^4$ computed from RPMD using primitive, NM, and staging coordinates. As the transformations were carried out canonically, the dynamical quantities should be reproduced exactly in the same manner as is shown in the figure. The minor discrepancies between curves are due to the sampling over different initial conditions. Note that if the correlation functions are generated from a single trajectory starting from exactly the same initial conditions (figure not shown), this small discrepancy disappears entirely.

F. Ergodicity problem in path integral simulations

Ergodicity is a problem that plagues both CMD and RPMD simulations.³² While we do not wish to affect the dynamics of the system, it is imperative to have adequate statistics. One possible way to satisfy these conflicting requirements is to employ a combined approach whereby a mild dissipative particle dynamics thermostat^{56,57} is used on the centroid and Langevin or Nosé–Hoover chain³⁷ thermostats are applied to the internal modes to achieve a rapid equilibration. This approach, however, was not pursued in this work. Rather, we focus our attention on the acquisition of averages and correlation functions.

In previous studies, averages were accumulated in a sequential manner starting from a limited portion of coordinate space and proceeding thereafter with only a resampling of the velocities. This protocol, although straightforward, may

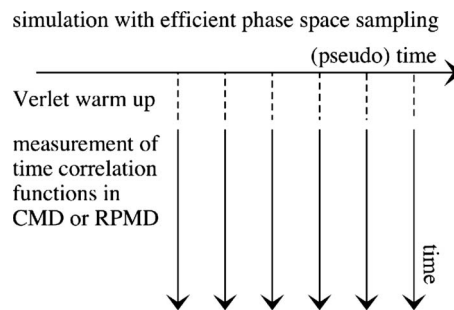


FIG. 2. Schematic representation of how to efficiently accumulate ergodic time correlation functions without distorting the dynamics during the observation stage.

be problematic due to the slow convergence of PIs in general, with particular severity near phase transitions.

In this study, an improved sampling method is proposed to ensure a proper sampling of configuration space. Figure 2 depicts the scheme. First, a long equilibrium PIMD simulation is performed, as described in Sec. II A, with the sole purpose of generating uncorrelated initial configurations. Since equilibrium PIMD algorithms normally work internally in staging or NM variables for optimal sampling, the periodically sampled configurations can then be used directly in the CMD simulations, and, for RPMD, they must be transformed back to primitive variables.

The initial velocities can be either drawn from the Maxwell–Boltzmann distribution or taken from the equilibrium PIMD run provided that a brief adjustment of the initial velocities is allowed (short equilibration or “Verlet warm up” in the figure) due to the different mass tensor in the dynamical algorithms. Periodic resampling of velocities may be employed in each individual trajectory to further improve statistics.

This sampling scheme allows for a more efficient exploration of configuration space and is expected to improve statistics as the averages become less correlated than the sequential method. A quantitative measure of the error associated with each sampling technique is given in Fig. 3 for a particle in a purely quartic potential. The figure displays

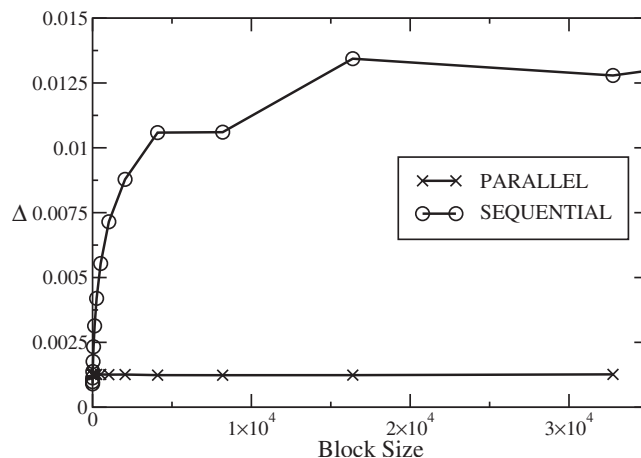


FIG. 3. Relative error in the mean Δ (defined in Ref. 58) of the virial estimator as a function of the block size for different sampling techniques in RPMD. Quartic potential $V(x)=0.25x^4$, $\beta=8$, and $P=32$. Circles: sequential sampling (previous works); crosses: suggested parallel sampling scheme.

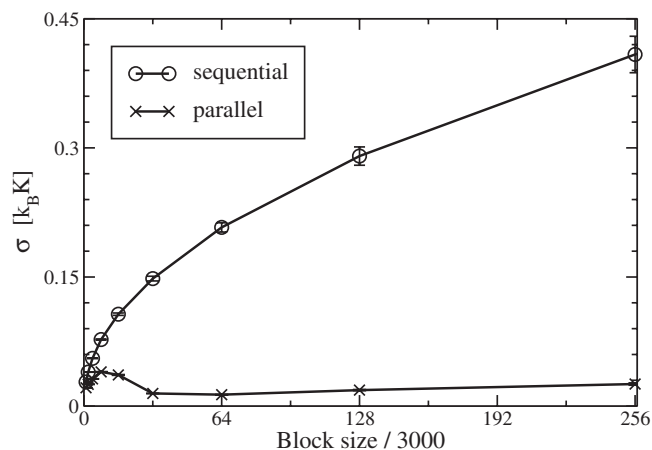


FIG. 4. Standard deviation of the virial estimator as a function of the block size for different sampling techniques in RPMD. Liquid *para*-hydrogen at $T=14$ K and $P=64$. The time step was 0.76 fs. Circles: sequential sampling (previous works); crosses: suggested parallel sampling scheme.

the relative error in the mean [see Eq. (2.3) of Ref. 58] for the virial estimator⁵⁹ as a function of block size (number of steps between two consecutive velocity-rescale updates). The total number of observation steps in each sampling scheme remains constant, only differing in the way steps are distributed. It is evident that the sequential sampling has about an order of magnitude greater error than the parallel sampling, which converges at the beginning and stays constant thereafter. These error magnitudes agree with those of Ref. 32.

The effect of the sampling method on the virial estimator was also investigated in a more realistic system. Figure 4 displays the results for liquid *para*-hydrogen near its triple point, $T=14$ K, $\rho=0.0235$ Å⁻³. The figure shows the more favorable convergence properties of the parallel sampling.

Finally, the rate of convergence of RPMD correlation functions versus number of trajectories was also investigated for each sampling method. Figure 5 displays the mean abso-

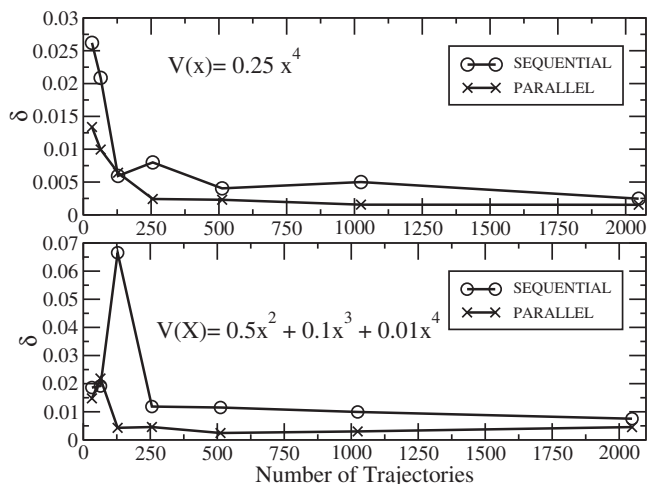


FIG. 5. Mean absolute error of the RPMD correlation functions $\delta = 1/N \sum_{i=1}^N |K_{xx}(t_i) - K_{xx}^{\text{conv}}(t_i)|$ for parallel and sequential sampling methods. K_{xx}^{conv} is the fully converged Kubo-transformed position autocorrelation function. Above: quartic $V(x)=0.25x^4$ potential. Below: mildly anharmonic $V(x)=0.5x^2+0.1x^3+0.01x^4$ potential. A inverse temperature $\beta=8$ and Trotter number $P=32$ were used in both model potentials. The number of steps per trajectory was 60 000 for each sampling method.

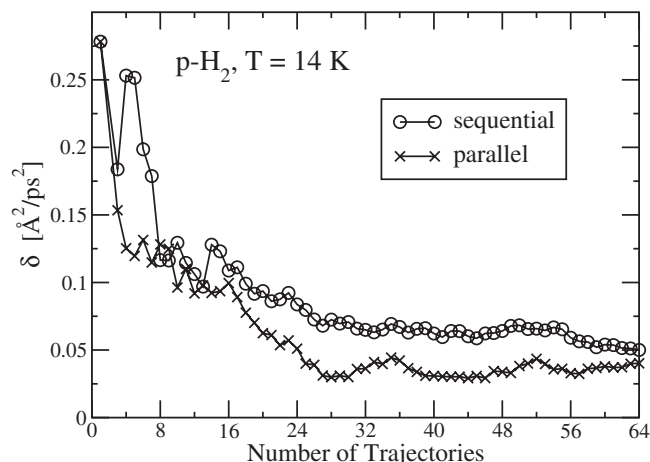


FIG. 6. Mean absolute error of the RPMD correlation functions, $\delta = 1/N \sum_{i=1}^N |K_{vv}(t_i) - K_{vv}^{\text{conv}}(t_i)|$, for parallel and sequential sampling methods. K_{vv}^{conv} is the fully converged Kubo-transformed velocity autocorrelation function for the *para*-hydrogen at $T=14$ K and $P=32$ obtained using RPMD. The number of steps per trajectory was 3500 and time step of 0.76 fs for each sampling method.

lute error $\delta = 1/N \sum_{i=1}^N |K_{xx}(t_i) - K_{xx}^{\text{conv}}(t_i)|$ of each sampling method for various model systems. K_{xx}^{conv} denotes the fully converged RPMD correlation function for the system, N is the total number of sampled points, and K_{xx} is the resulting correlation function obtained from the cumulative average over consecutive trajectories (sequential sampling) or from statistically independent trajectories (parallel sampling). The difference was computed up to a maximum time of $t_{\text{max}} = 10$ a.u. (longer times comparisons are not meaningful) for the one dimensional systems. The total simulation time was equal for each sampling method for consistency. As a general trend, parallel sampling not only exhibits less statistical error associated but also converges faster than sequential sampling.

Similarly, Fig. 6 illustrates the impact of the sampling technique on the RPMD velocity autocorrelation function for liquid *para*-hydrogen at the same physical conditions given above. The difference was computed up to a maximum time of $t_{\text{max}} = 1$ ps. The sequential sampling curve is always above the parallel curve, indicating that the even for this more ergodic system the parallel sampling is useful. Thus, the parallel sampling technique is recommended as a method for generating converged dynamical quantities, especially in cases where ergodicity problems are expected.

G. Self-consistent quality control of time correlation functions

As argued in Sec. I, it is desirable to have an internal consistency check for the predicted time correlation functions without relying on exact data (often not available in complex systems). From the simulations (whether CMD or RPMD) and using Eq. (14) one obtains approximations to the standard velocity autocorrelation function $\tilde{C}_{vv}(\omega)$, which we denote by $\tilde{C}_{vv}^{(\text{est})}(\omega)$. Equation (17) allows us to reconstruct the associated imaginary time correlation function $G^{(\text{est})}(\tau)$ from $\tilde{C}_{vv}^{(\text{est})}(\omega)$. The estimated $G^{(\text{est})}(\tau)$ function can then be compared directly to the numerically exact mean

square displacement function $G(\tau)$ computed from the same simulation (see Eq. (16)). Thus, a dimensionless quantitative descriptor for the quality of an approach (CMD/RPMD) would be

$$\chi^2 = \frac{1}{\beta\hbar} \int_0^{\beta\hbar} d\tau \left[\frac{G^{(\text{est})}(\tau) - G(\tau)}{G(\tau)} \right]^2. \quad (32)$$

An alternative method for carrying out this comparative test is to compare directly and on the same footing the numerically sampled imaginary time velocity autocorrelation function (ITVACF) $G_{vv}(\tau)$, Eq. (15) (see Ref. 28 and also Eq. A2 in Ref. 30 for a lowest-order estimator) to the one reconstructed from the real-time velocity autocorrelation function using a similar expression as Eq. (17), but without the division by ω^2 ,

$$G_{vv}(\tau) = \frac{1}{2\pi} \int_{-\infty}^{\infty} d\omega \exp(-\beta\hbar\omega/2) \tilde{C}_{vv}(\omega) \times \cosh \left[\omega \left(\frac{\beta\hbar}{2} - \tau \right) \right]. \quad (33)$$

We have carried out this comparison as well (see Fig. 12 in Sec. IV) and, in practice, we find the two self-consistency tests are equivalent in what they reveal about the quality of the approximate real-time correlation functions.

III. COMPUTATIONAL DETAILS

In this section, we present the computational details for the model systems investigated. For the one dimensional model systems, a total of 2048 independent trajectories of 130 natural units of time each were accumulated, according to the scheme depicted in Fig. 2. Ten restarts on each individual trajectory are effected to further improve the statistics. The Trotter numbers were 8 and 32 for the high and low temperatures, respectively. For CMD, a converged adiabaticity parameter $\gamma^2=0.005$ was used in all the low dimensional systems to scale down the noncentroid kinetic masses. The time step (after adiabatic separation) was 0.001. Nosé–Hoover chain thermostats³⁷ of length 2 were employed on the internal (noncentroid) modes to achieve proper canonical sampling. In the RPMD simulations, the time step was 0.0005 to properly integrate all internal modes.

A realistic quantum fluid, *para*-hydrogen, was also simulated. The physical conditions of the system were chosen near its triple point ($T=14$ K, $\rho=0.0235$ Å⁻³) to facilitate the comparison to preceding studies.^{51,22} As usual, boson exchange effects are neglected at this temperature. The interaction between hydrogen molecules was modeled using the well-known isotropic Silvera–Goldman (SG) potential.⁶⁰ This potential is given by

$$V(r) = e^{\alpha-\beta r-\gamma r^2} - \left(\frac{C_6}{r^6} + \frac{C_8}{r^8} - \frac{C_9}{r^9} + \frac{C_{10}}{r^{10}} \right) f_c(r), \quad (34)$$

where

TABLE I. Parameters (in a.u.) in the SG potential, Eq. (34).

α	1.713
β	1.5671
γ	0.009 93
r_c	8.321
C_6	12.14
C_8	215.2
C_9	143.1
C_{10}	4813.9

$$f_c(r) = \begin{cases} \exp \left[- \left(\frac{r_c}{r} - 1 \right)^2 \right], & \text{if } r \leq r_c \\ 1, & \text{otherwise.} \end{cases}$$

The parameters (in atomic units) for the SG potential are displayed in Table I. This potential has been shown to reproduce accurately static and dynamic properties in both solid and liquid phases.⁶¹

The system was composed of 256 particles initially arranged in a fcc lattice with periodic boundary conditions. The minimum image convention was adopted for the intermolecular interactions. The interaction between *para*-hydrogen molecules was truncated at 8.374 Å, corresponding to the second minimum in the radial distribution function. Initial velocities were drawn from a Maxwell–Boltzmann distribution at every restart to explore momenta space. A Trotter number of $P=32$ was sufficient to converge energy estimators at these physical conditions within a 97% margin of error. A full convergence of thermodynamic quantities is not sought here. Rather, we aim to compare the performance of each imaginary time PI method under the same simulation parameters.

Canonical sampling was achieved via Langevin thermostats. Although stochastic thermostats pose serious problems in the calculation of dynamical properties, they are very effective for rapid equilibration. In this study, the friction parameter Γ was carefully chosen so as not to disrupt the dynamical properties of the system. A friction coefficient of $\Gamma = 0.01/dt$ typically makes systematic errors smaller than statistical errors.³¹ No thermostats were directly applied to the centroids during CMD runs.

For CMD, the time scale separation between centroid and internal modes was set to 15 (adiabaticity parameter $\gamma^2 = 0.0444$) and the time step to 0.2 fs. In order to facilitate exploration of configurational space, 128 independent trajectories were run for both methods with two restarts on each, following the scheme depicted in Fig. 2, giving a total of 256 trajectories. The duration of each trajectory was 6 ps. The time step used in RPMD was 0.76 fs to properly integrate all internal modes and ensure conservation of the total energy.

IV. RESULTS AND DISCUSSION

A. One dimensional model potentials

Figures 7 and 8 show the Kubo-transformed position autocorrelation functions for the mildly anharmonic and quartic potential, respectively. To facilitate comparisons to literature,

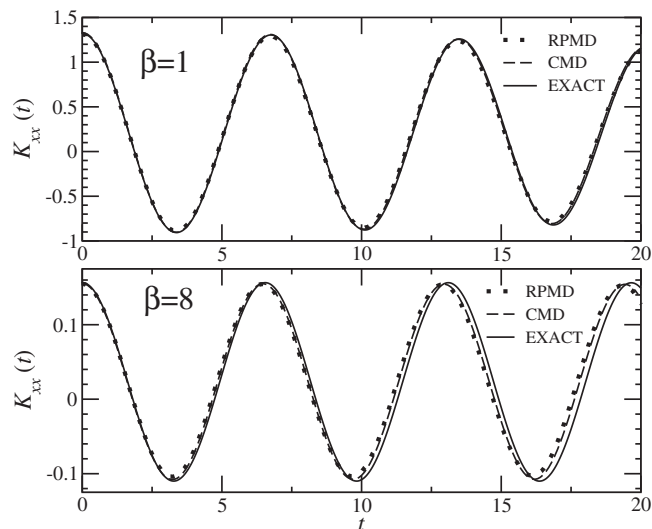


FIG. 7. Kubo-transformed position autocorrelation functions for the mildly anharmonic potential $V(x)=0.5x^2+0.1x^3+0.01x^4$ at two different temperatures.

the same inverse temperatures used in previous studies were employed here, namely, $\beta=1$ and 8, respectively.^{19,22}

In general, the CMD and RPMD correlation functions agree well with each other and with exact results at times less than the thermal time. As expected, the agreement between CMD and the exact curves improves as the adiabatic separation between centroid and internal modes is increased (not shown).

In the harmonic limit both methods are exact (at all times). Figure 7 illustrates this point by showing the results on a slightly perturbed harmonic system. At high temperature ($\beta=1$) the agreement with exact curve is excellent in both methods. At lower temperature ($\beta=8$) however, the agreement is less satisfactory, with RPMD dephasing slightly more than the CMD at long times.

In anharmonic systems, CMD and RPMD suffer from a progressive loss of coherence and intensity as time goes on,

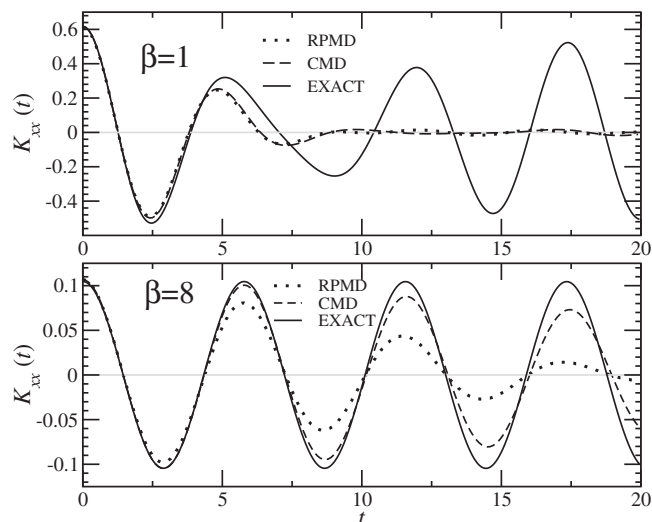


FIG. 8. Comparison of the Kubo-transformed position autocorrelation function for the purely quartic potential $V(x)=0.25x^4$ at two different temperatures.

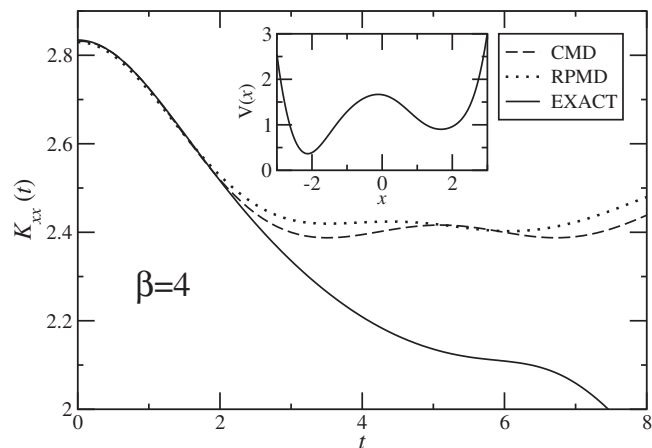


FIG. 9. Comparison of the Kubo-transformed position autocorrelation function for an asymmetric double well potential $V(x)=0.1(x^2-2)^2+e^{-(x-2.2)^2}+0.5e^{-(x+1.5)^2}$ at $\beta=4$ and $P=32$: exact (solid), RPMD (dots), and adiabatic CMD (dashes). The bare potential is shown in the inset.

which is especially significant for the quartic case at $\beta=1$, Fig. 8, where both methods are dramatically quenched after the first oscillation.

At low temperatures, the quantum effects are more pronounced and both methods are expected to perform less favorably. Nonetheless, for the quartic case, the dynamics is curiously better described at low temperatures, whereas at high temperature the behavior is opposite. As pointed out by Voth and co-workers,^{15,22,62} this behavior can be ascribed to the two-state nature of the system. At low temperature, the dynamics of the system is mostly dominated by the ground and first excited state. Therefore, it exhibits an effective harmonic behavior for which both approximate methods are exact. Interestingly, the quartic potential at $\beta=8$, Fig. 8 shows that CMD can sustain oscillations longer than RPMD, which is severely quenched after few oscillations. The RPMD curve resembles the CMD signal but with the amplitude modulated by a decay function that results from the dephasing of the individual trajectories at long times. This interesting effect can be easily explained by the following phenomenological argument. In RPMD the centroid dynamics contains an admixture of higher frequencies modes (see later discussion on the power spectrum of a quantum fluid) which results in more damped behavior in the time correlation functions after averaging. Thus, each individual RPMD trajectory loses coherence more rapidly than CMD as time progresses.

Finally, a more challenging model potential for these approximate methods was also investigated. Figure 9 shows the Kubo-transformed position autocorrelation function of an asymmetric double well potential at $\beta=4$. This potential crudely represents the typical scenario for a reduced coordinate in the vicinity of a quantum phase transition. As with any method that neglects quantum interference, neither RPMD nor CMD are able to describe the coherence in this deep tunneling case and the dynamics remains accurate only at very short times.

It should be pointed out that the dynamics in condensed phases is often dominated by the short-time behavior of cor-

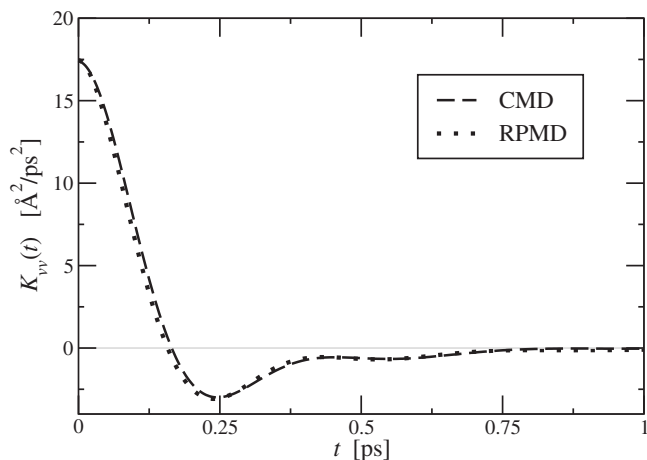


FIG. 10. Kubo-transformed velocity autocorrelation function for *para*-hydrogen at $T=14$ K, $\rho=0.0235$ \AA^{-3} as computed from adiabatic CMD (dashes) and RPMD (dots).

relation functions (provided that the density/pressure is not too high) and these methods are expected to become more meaningful as is illustrated in Sec. IV B.

B. Liquid *para*-hydrogen

In this section, the comparative study of a realistic quantum fluid system is presented. Figure 10 displays the Kubo-transformed velocity autocorrelation function for *para*-hydrogen. Both correlation functions look very similar, and feature a prominent negative minimum at about 0.24 ps, a little bump around 0.4 ps, followed by a fast decay after 1 ps. The RPMD curve is, however, noticeably displaced to the left relative to the CMD curve. This observation is consistent with the general trend of RPMD correlation functions to relax faster than CMD (see following discussion on diffusion constants). Table II displays the values of the velocity autocorrelation function at few selected points for each method.

Table III lists the values of the self-diffusion coefficient for *para*-hydrogen computed from the well-known Green-Kubo relation⁴⁵

$$D = \frac{1}{3} \int_0^{\infty} K_{vv}(t) dt. \quad (35)$$

Values in Table III are in accord with previously reported data.^{22,51} In particular, the predicted RPMD value (0.263 $\text{\AA}^2/\text{ps}$) is in excellent agreement with a recent study

TABLE II. The Kubo-transformed velocity autocorrelation function ($\text{\AA}^2/\text{ps}^2$) at various selected points for *para*-hydrogen at $T=14$ K, $\rho=0.0235$ \AA^{-3} with $N=256$. The standard deviation in the last digit is given in parentheses.

Time (ps)	CMD	RPMD
0.0	17.45(3)	17.46(2)
0.156	0.94(2)	0.41(1)
0.238	-2.96(1)	-3.07(1)
0.50	-0.61(1)	-0.66(1)
0.751	-0.15(1)	-0.14(1)

TABLE III. Self-diffusion coefficient for *para*-hydrogen at $T=14$ K, $\rho=0.0235$ \AA^{-3} with $N=256$ as computed from PI methods. The experimental value is from Ref. 64. The standard deviation in the last digit is given in parentheses.

	Diffusion coefficient D ($\text{\AA}^2/\text{ps}$)
Experiment	0.4
CMD	0.306(2)
RPMD	0.263(1)

by Miller and Manolopoulos.⁵¹ Our CMD value for the self-diffusion constant agrees very well with the one reported in Ref. 22 and the small discrepancy (around 0.01) is attributed to different simulation parameters. As a consistency check, the diffusion constants were also estimated from the long-time behavior of the mean square displacement (not shown) and were found to be in perfect agreement with those from Eq. (35). Finally, we note that these computed diffusion coefficients should be extrapolated to the thermodynamic limit for better agreement with the experiment.⁵¹ Conversely, the experimental value could also be “corrected” for finite size effects⁶³ and then compared directly to the values from the simulations.

Figure 11 shows the imaginary time correlation function, Eq. (16), and its reconstructed version [computed from Eq. (17)] for each PI method. The imaginary time mean square displacement (ITMSD) function (“ima,” in the figure) is virtually identical in both RPMD and CMD, indicating a converged sampling. The reconstructed RPMD ITMSD (dots) appears to be slightly farther than CMD (dashes) from its respective imaginary time correlation function. Equation (17) was used to quantify this difference, and the numerical values for χ^2 (0.0089 for RPMD and 0.0056 for CMD) are also presented in Fig. 11. RPMD exhibits a slightly poorer convergence than CMD under the same simulation parameters (total observed time, etc).

Figure 12 shows the ITVACF comparison for each PI method. Our results agree very well with the ones reported in

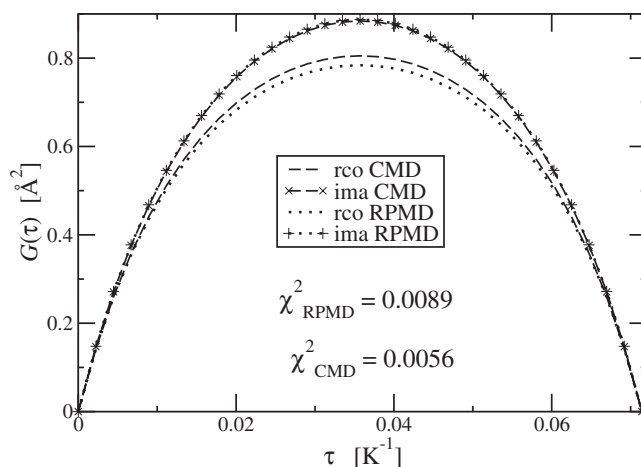


FIG. 11. Comparison of the ITMSD correlation function (ima, in the figure) as given by Eq. (16), and its reconstructed version (“rco” in the figure) from Eq. (17) for *para*-hydrogen at $T=14$ K, $\rho=0.0235$ \AA^{-3} . The χ^2 error as defined in Eq. (32) is shown for each method.

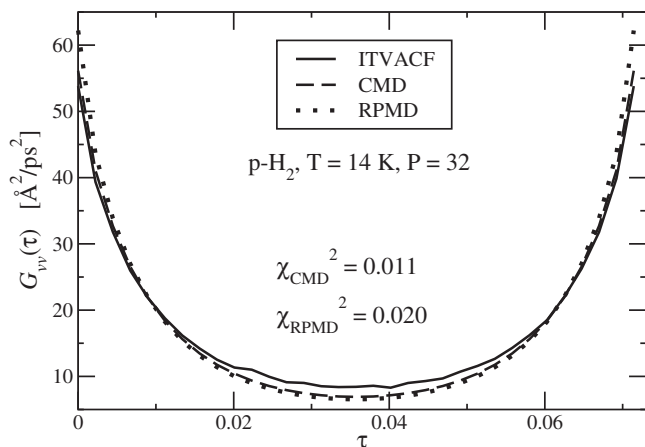


FIG. 12. Comparison of the ITVACF (“ITVACF,” in the figure) as given by Eq. (15), and its reconstructed version from Eq. (33) for *para*-hydrogen at $T=14$ K, $\rho=0.0235$ Å⁻³. The χ^2 error as defined in Eq. (32) is shown for each method.

literature (see, for example, Ref. 28 and also Fig. 8 in the work by Habershon *et al.*³⁰). Basically, CMD and RPMD perform similarly although RPMD slightly overestimates the value of the “exact” ITVACF at the end points and underestimates its value at the middle of the thermal interval, as already noticed by Habershon *et al.*³⁰ CMD with a $\chi^2=0.011$, on the other hand, seems to be a little closer than RPMD ($\chi^2=0.020$) to the numerically sampled ITVACF.

As a further investigation of the differences between both methods, the Fourier transform of the real-time velocity autocorrelation function²²

$$\tilde{C}_{vv}(\omega) = \int_{-\infty}^{\infty} C_{vv}(t) e^{i\omega t} dt, \quad (36)$$

was computed for *para*-hydrogen and its real part is shown in Fig. 13. In both methods, the spectra look very similar at low and mid frequencies and features a strong asymmetric peak at 75 cm⁻¹. The only difference arises at higher frequencies. This fact provides some insight into the physical

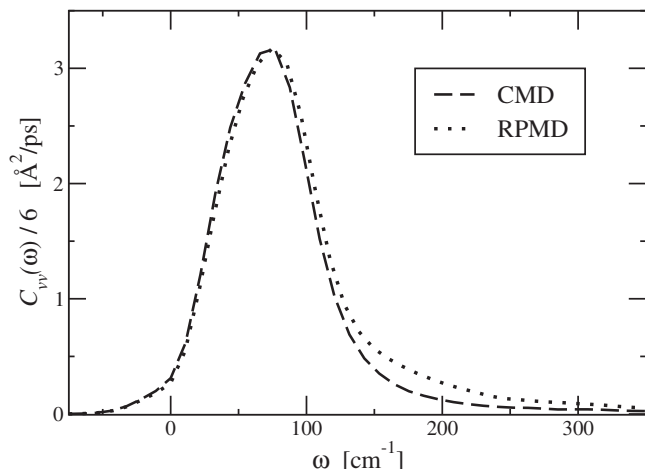


FIG. 13. Comparison of the computed Fourier transform of the standard velocity autocorrelation function for *para*-hydrogen at $T=14$ K, $\rho=0.0235$ Å⁻³. To facilitate comparisons, the same scale was used on the y-axis as in Fig. 5 of Ref. 22. Only the real part is shown.

difference between the PI methods. The RPMD spectrum reveals a significant presence of high-frequency centroid vibrations (due to undamped internal modes) as already pointed out by Hone *et al.*²² This has a direct effect on the centroid dynamics causing a faster relaxation in the correlation functions and thereby leading to a smaller value for the self-diffusion constants (Table III). In contrast, in CMD, the effect of the thermostats on the internal modes results in a smoother centroid dynamics and hence, less damping in the correlation functions. This results in a slightly better reconstructed imaginary time correlation functions and hence a somewhat smaller χ^2 error.

V. CONCLUSIONS

In this paper, we have addressed the problem of ergodic sampling in the centroid and RPMD techniques, and we have introduced an internal consistency descriptor χ^2 for assessing the accuracy of the approximate quantum time correlation functions. In addition, we have discussed the physical differences between imaginary time PI methods, CMD and RPMD. These methods were compared numerically for a variety of model systems using an improved sampling technique to remedy any potential nonergodic behavior. The computed values from linear correlation functions are very similar in condensed phases (*para*-hydrogen), and both methods yield similar performance in recovering imaginary time correlation functions. Overall, our comparison indicates that both methods perform essentially the same in recovering dynamical information. However, in less ergodic systems such as the purely quartic system at low temperature, the approximate methods differ significantly. In this model system, the resulting RPMD correlation function exhibits more damped behavior due to effect of internal modes on the centroid motion. In contrast, this effect is less severe in CMD owing to the averaging effect of the thermostats on the high-frequency modes of the ring polymer.

ACKNOWLEDGMENTS

The authors would like to thank Serge Ivanov for critical reading on an early draft of this manuscript, Dominik Marx for helpful comments, Debashish Mukherji for help with the RPMD code, and the anonymous reviewers for their valuable comments. M.E.T. acknowledges support from NSF under Grant No. CHE-0704036. M.H.M. acknowledges financial support from NSERC and PREA.

- ¹R. P. Feynman, *Rev. Mod. Phys.* **20**, 367 (1948).
- ²R. P. Feynman, *A New Approach to Quantum Theory (Feynman's Thesis)*, edited by L. M. Brown (World Scientific, Singapore, 2005).
- ³D. M. Ceperley, *Rev. Mod. Phys.* **67**, 279 (1995).
- ⁴J. Liu and W. H. Miller, *J. Chem. Phys.* **127**, 114506 (2007).
- ⁵J. Liu and W. H. Miller, *J. Chem. Phys.* **128**, 144511 (2008).
- ⁶D. R. Reichman and E. Rabani, *Phys. Rev. Lett.* **87**, 265702 (2001).
- ⁷E. Rabani and D. R. Reichman, *Annu. Rev. Phys. Chem.* **56**, 157 (2005).
- ⁸E. Rabani and D. R. Reichman, *Phys. Rev. E* **65**, 036111 (2002).
- ⁹D. R. Reichman and E. Rabani, *J. Chem. Phys.* **116**, 6279 (2002).
- ¹⁰E. Rabani and D. R. Reichman, *J. Chem. Phys.* **120**, 1458 (2004).
- ¹¹A. Nakayama and N. Makri, *J. Chem. Phys.* **119**, 8592 (2003).
- ¹²A. Nakayama and N. Makri, *J. Chem. Phys.* **125**, 024503 (2006).
- ¹³J. A. Poulsen, G. Nyman, and P. J. Rossky, *Proc. Natl. Acad. Sci. U.S.A.* **102**, 6709 (2005).

- ¹⁴ A. Horikoshi and K. Kinigawa, *J. Chem. Phys.* **119**, 4629 (2003).
- ¹⁵ J. Cao and G. A. Voth, *J. Chem. Phys.* **99**, 10070 (1993).
- ¹⁶ J. Cao and G. A. Voth, *J. Chem. Phys.* **100**, 5106 (1994).
- ¹⁷ H. Kim and P. J. Rossky, *J. Phys. Chem. B* **106**, 8240 (2002).
- ¹⁸ H. Kim and P. J. Rossky, *J. Chem. Phys.* **125**, 074107 (2006).
- ¹⁹ I. R. Craig and D. E. Manolopoulos, *J. Chem. Phys.* **121**, 3368 (2004).
- ²⁰ M. Parrinello and A. Rahman, *J. Chem. Phys.* **80**, 860 (1984).
- ²¹ B. J. Braams and D. E. Manolopoulos, *J. Chem. Phys.* **125**, 124105 (2006).
- ²² T. D. Hone, P. J. Rossky, and G. A. Voth, *J. Chem. Phys.* **124**, 154103 (2006).
- ²³ R. M. Lynden-Bell and K. H. Michel, *Rev. Mod. Phys.* **66**, 721 (1994).
- ²⁴ M. Holz, X. Mao, D. Seiferling, and A. Sacco, *J. Chem. Phys.* **104**, 669 (1996).
- ²⁵ G. Baym and D. N. Mermin, *J. Math. Phys.* **2**, 232 (1961).
- ²⁶ B. J. Berne and D. Thirumalai, *Annu. Rev. Phys. Chem.* **37**, 401 (1986).
- ²⁷ E. Rabani, G. Krilov, and B. J. Berne, *J. Chem. Phys.* **112**, 2605 (2000).
- ²⁸ E. Rabani, D. R. Reichman, G. Krilov, and B. J. Berne, *Proc. Natl. Acad. Sci. U.S.A.* **99**, 1129 (2002).
- ²⁹ E. Rabani, G. Krilov, D. R. Reichman, and B. J. Berne, *J. Chem. Phys.* **123**, 184506 (2005).
- ³⁰ S. Habershon, B. J. Braams, and D. E. Manolopoulos, *J. Chem. Phys.* **127**, 174108 (2007).
- ³¹ F. R. Krajewski and M. H. Müser, *J. Chem. Phys.* **122**, 124711 (2005).
- ³² M. E. Tuckerman, B. J. Berne, G. J. Martyna, and M. L. Klein, *J. Chem. Phys.* **99**, 2796 (1993).
- ³³ R. P. Feynman and A. R. Hibbs, *Quantum Mechanics and Path Integrals* (McGraw-Hill, New York, 1965).
- ³⁴ D. Chandler and P. G. Wolynes, *J. Chem. Phys.* **74**, 4078 (1981).
- ³⁵ R. W. Hall and B. J. Berne, *J. Chem. Phys.* **81**, 3641 (1984).
- ³⁶ E. L. Pollock and D. M. Ceperley, *Phys. Rev. B* **30**, 2555 (1984).
- ³⁷ G. J. Martyna, M. L. Klein, and M. E. Tuckerman, *J. Chem. Phys.* **97**, 2635 (1992).
- ³⁸ J. S. Cao and G. A. Voth, *J. Chem. Phys.* **101**, 6168 (1994).
- ³⁹ M. E. Tuckerman, D. Marx, M. L. Klein, and M. Parrinello, *J. Chem. Phys.* **104**, 5579 (1996).
- ⁴⁰ D. Marx, M. E. Tuckerman, and G. J. Martyna, *Comput. Phys. Commun.* **118**, 166 (1999).
- ⁴¹ G. J. Martyna, A. Hughes, and M. E. Tuckerman, *J. Chem. Phys.* **110**, 3275 (1999).
- ⁴² M. H. Musër, *Comput. Phys. Commun.* **147**, 83 (2002).
- ⁴³ L. D. Landau and E. M. Lifshitz, *Statistical Physics* (Pergamon, New York, 1968).
- ⁴⁴ D. Thirumalai, E. J. Bruskin, and B. J. Berne, *J. Chem. Phys.* **79**, 5063 (1983).
- ⁴⁵ R. Kubo, M. Toda, and N. Hashitsume, *Statistical Physics II: Nonequilibrium Statistical Mechanics* (Springer, New York, 1985).
- ⁴⁶ R. P. Feynman and H. Kleinert, *Phys. Rev. A* **34**, 5080 (1986).
- ⁴⁷ M. J. Gillan, *J. Phys. C* **20**, 3621 (1987).
- ⁴⁸ J. Cao and G. A. Voth, *J. Chem. Phys.* **104**, 273 (1996).
- ⁴⁹ J. Cao and G. J. Martyna, *J. Chem. Phys.* **104**, 2028 (1996).
- ⁵⁰ R. Hernandez, J. S. Cao, and G. A. Voth, *J. Chem. Phys.* **103**, 5018 (1995).
- ⁵¹ T. F. Miller III and D. E. Manolopoulos, *J. Chem. Phys.* **122**, 184503 (2005).
- ⁵² T. F. Miller III and D. E. Manolopoulos, *J. Chem. Phys.* **123**, 154504 (2005).
- ⁵³ I. R. Craig and D. E. Manolopoulos, *Chem. Phys.* **322**, 236 (2006).
- ⁵⁴ I. R. Craig and D. E. Manolopoulos, *J. Chem. Phys.* **122**, 084106 (2005).
- ⁵⁵ M. E. Tuckerman, B. J. Berne, and G. J. Martyna, *J. Chem. Phys.* **97**, 1990 (1992).
- ⁵⁶ T. Soddemann, B. Dünweg, and K. Kremer, *Phys. Rev. E* **68**, 046702 (2003).
- ⁵⁷ P. Nikunen, M. Karttunen, and I. Vattulainen, *Comput. Phys. Commun.* **153**, 407 (2003).
- ⁵⁸ J. Cao and B. J. Berne, *J. Chem. Phys.* **91**, 6359 (1989).
- ⁵⁹ M. F. Herman, E. J. Bruskin, and B. J. Berne, *J. Chem. Phys.* **76**, 5150 (1982).
- ⁶⁰ I. F. Silvera and V. V. Goldman, *J. Chem. Phys.* **69**, 4209 (1978).
- ⁶¹ D. Scharf, G. J. Martyna, and M. L. Klein, *Low Temp. Phys.* **19**, 364 (1993).
- ⁶² S. Jang and G. A. Voth, *J. Chem. Phys.* **111**, 2371 (1999).
- ⁶³ I. C. Yeh and G. Hummer, *J. Phys. Chem. B* **108**, 15873 (2004).
- ⁶⁴ *Properties of Liquid and Solid Hydrogen*, edited by B. N. Eselson, Y. P. Blagoi, V. V. Geigoriev, V. G. Manzheli, S. A. Mikhailenko, and N. P. Neklyndov (Israel Program for Scientific Translation, Jerusalem, 1971).
- ⁶⁵ A. Witt, S. D. Ivanov, M. Shiga, H. Forbert, and D. Marx, *J. Chem. Phys.* (in press).